applied optics

Eye-safe fiber laser for long-range 3D imaging applications

Lars G. Holmen,[1,2,*] Gunnar Rustad,[1] and Magnus W. Haakestad[1,2]

[1]Norwegian Defence Research Establishment (FFI), P.O. Box 25, NO-2027 Kjeller, Norway
[2]Department of Technology Systems, University of Oslo, P.O. Box 70, NO-2027 Kjeller, Norway
*Corresponding author: Lars.Holmen@ffi.no

Received 15 June 2018; revised 13 July 2018; accepted 13 July 2018; posted 13 July 2018 (Doc. ID 332379); published 7 August 2018

We report an all-fiber Er/Yb master oscillator power amplifier at 1.55 μm, delivering 135 μJ pulses with 6 ns duration (full width at half-maximum) at 100 kHz pulse repetition frequency, limited by stimulated Brillouin scattering. The output contains <1% amplified spontaneous emission and has a beam quality of $M^2 = 1.1$. By seeding with a high-power distributed-feedback laser diode, only two fiber amplification stages are needed, which represents a low overall system complexity compared to reported sources of similar performance. With an optical-to-optical efficiency of 29% and a robust alignment-free design, the source is well suited for field applications in 3D imaging with a several-kilometer range, and we present results from using it in an in-house-developed scanning lidar system.

OCIS codes: (060.2320) Fiber optics amplifiers and oscillators; (140.3538) Lasers, pulsed; (120.0280) Remote sensing and sensors; (280.3640) Lidar.

https://doi.org/10.1364/AO.57.006760

1. INTRODUCTION

Lidar (light detection and ranging) is becoming an increasingly prominent active electro-optical sensing method with applications in, e.g., three-dimensional mapping, autonomous navigation, and object identification [1,2]. The laser source is a determining performance factor in a lidar system, and recent technological progress has made fiber lasers attractive for use in such systems because of their robustness, operational flexibility, and high efficiency [2,3]. Although being limited in peak power due to nonlinear optical effects, fiber lasers are good candidates for use in high-repetition-rate scanning lidar systems with a several-kilometer detection range, where moderate pulse energies around 100 μJ are required at several tens of kilohertz pulse repetition frequency.

Fiber lasers and lidar systems operating at the "eye-safe" wavelength of 1.55 μm are becoming widespread, where the development benefits from the mature technology of telecommunications for both sources and detectors [3]. The most common source architecture is that of master oscillator power amplifiers (MOPAs), which allows for operational flexibility by choosing a suitable seed laser (e.g., a gain-switched diode laser) and power scalability by using a series of fiber amplifiers.

Several 1.55 μm nanosecond-pulsed fiber amplifiers have been demonstrated the last decade, with pulse energies typically between hundreds of microjoules and a few millijoules [4–11]. Energy scaling in the reported sources is normally limited by either amplified spontaneous emission or nonlinear effects, where the latter is particularly important for narrow-linewidth amplifiers that are sensitive to stimulated Brillouin scattering. An all-fiber MOPA delivering pulses of 5 ns duration, 100 μJ energy, and 100 kHz pulse repetition frequency with single-mode beam quality was reported [5]; however, this was an intricate system consisting of five amplification stages. Several less complex sources with high performance have been demonstrated, but also these would have drawbacks as practical field instruments in a long-range scanning lidar system due to factors such as large contents of amplified spontaneous emission (ASE) [6,8], long pulse durations above 100 ns [4,7,11], optical-to-optical efficiency below 10% [6,9,11], poor beam quality [10], or bulk optics as part of the setup [6]. A robust all-fiber MOPA used in a scanning lidar was demonstrated [12] but was limited in pulse energy to 9 μJ.

In this paper, we present a simple and robust all-fiber 1.55 μm MOPA with high optical performance tailored to applications in eye-safe long-range 3D lidar imaging. By using a high-power distributed-feedback (DFB) diode laser as the seed source, we limit the system complexity to two stages of amplification, while achieving 135 μJ at 100 kHz pulse repetition frequency. To the best of our knowledge, this is the highest energy achieved for nanosecond pulses from a diode-seeded 1.55 μm MOPA containing only two amplification stages. We consider important design requirements for the laser source in the context of 3D lidar imaging at the several-km range and

present results from operating the MOPA in an in-house-developed scanning lidar system.

2. LASER SOURCES FOR LONG-RANGE LIDAR SYSTEMS

Many of the requirements for a laser source used in lidar applications depend on the type of lidar system, and the following discussion is based on the assumption of an incoherent scanning lidar using a single point detector in linear detection mode.

Atmospheric transmittance becomes increasingly important when extending the range of a remote sensing system. There exist several wavelength bands with high transmission where good fiber laser sources are available, such as around 1 μm (ytterbium), 1.5 μm (erbium), and 2 μm (thulium and holmium). Although the highest performance is currently available from Yb-doped fiber lasers, wavelengths above 1.4 μm are particularly attractive from eye safety considerations [2]. Figure 1 shows the absorption coefficient in air around 1.55 μm computed using *HITRAN on the web* [13]. Wavelength control and stabilization are clearly important in order to avoid absorption lines in this spectral region, but several available wavelengths without considerable attenuation are observed.

It is noted that long wavelengths are preferred also from considerations of atmospheric visibility, which is known to increase with wavelength in cases where attenuation is dominated by scattering from particles smaller or comparable in size to the wavelength [14]. This corresponds to conditions of high visibility (more than a few km). The advantage is, however, reduced and eventually disappears in low-visibility conditions (mist or fog) where attenuation is dominated by wavelength-independent scattering from larger particles [14].

The pulse energy required to achieve a certain detection range can be estimated from signal-to-noise considerations for a relevant detector technology in conjunction with the lidar range equation [15]. The choices of various parameters used in the following calculations are based on assumptions of realistic atmospheric conditions, state of the art InGaAs avalanche photodiode (APD) detectors, and reasonable specifications of a practical detection system.

We first assume a pulse length $\tau = 10$ ns and a corresponding electronic detection bandwidth $B = 1/(2\tau) = 50$ MHz. A range precision at the meter level or better is expected in this situation if using suitable signal processing of the return waveforms [16]. Although shorter pulses can be desirable for high range resolution, this implies higher peak powers, which is normally the limiting factor for pulsed fiber-based laser sources. Current commercially available InGaAs APDs have noise equivalent power (NEP) around 150 fW/$\sqrt{\text{Hz}}$, which gives a noise power of 1 nW for the assumed detection bandwidth. By requiring a signal-to-noise ratio (SNR) of 5 and assuming a square pulse shape, a received energy detection threshold of 50 aJ is computed, which corresponds to ∼400 photons at 1.55 μm wavelength.

The received power from a Lambertian target at a distance z is related to the transmitted power through the lidar range equation [3], which when written in terms of pulse energy reads

$$E_r = E_t \frac{D^2 \rho}{4z^2} \eta_{\text{atm}} \eta_{\text{sys}}. \tag{1}$$

Here, E_r and E_t are the received and transmitted pulse energies, respectively, D is the receiver diameter, ρ is the target reflectivity, and η_{atm} and η_{sys} are terms accounting for atmospheric and optical system efficiencies. We assume $\eta_{\text{sys}} = 1$, while the double-pass atmospheric transmittance is expressed as $\eta_{\text{atm}} = \exp(-3.91 \times 2z/V)$, where the visibility V is defined in the conventional manner as the range where light at the laser wavelength is attenuated to 2% of the original power [14].

Assuming a receiver aperture diameter of 5 cm and a target reflectance of 10%, we compute the required pulse energies for obtaining a return signal of 400 photons for atmospheric visibilities ranging from 5 km to infinity. The results are shown in Fig. 2, where it is evident that several tens of μJ are needed to achieve detection ranges of a few kilometers, and hence that 100 μJ is a relevant target energy for long-range lidar applications.

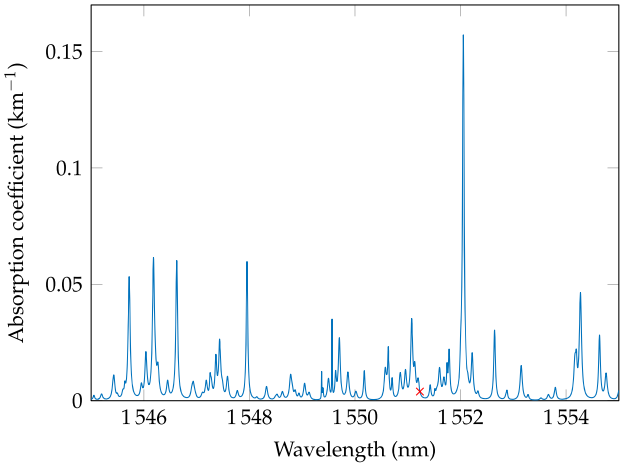

Fig. 1. Absorption coefficient computed using *HITRAN on the web* [13] for the "USA, mean latitude, summer" atmosphere model. The red cross shows the operating wavelength of our MOPA at 1551.23 nm (vacuum).

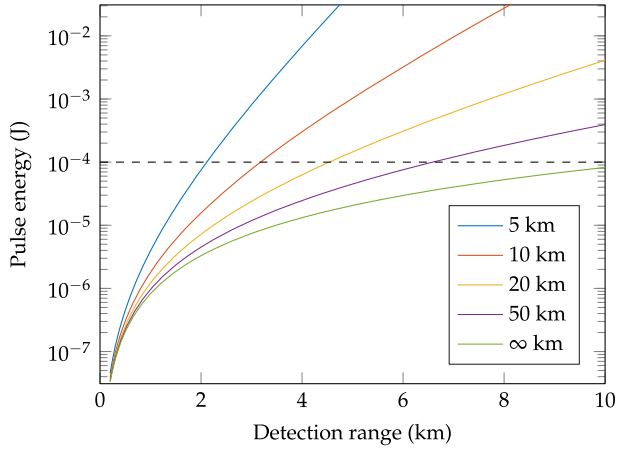

Fig. 2. Minimum energy in transmitted pulses in order to receive 400 photons from a 10% reflecting target for different atmospheric visibilities as indicated in the legend. A dashed line is drawn at 100 μJ.

For significantly longer distances or under conditions of low visibility, pulse energies at the mJ level or higher are required, which is not readily obtained from nanosecond-pulsed fiber amplifiers.

In addition to the importance of operating at an appropriate wavelength with sufficient pulse energy, a high pulse repetition frequency of several tens of kHz and higher is desirable in a scanning lidar because this will correspond to the pixel rate. Also, the beam quality should be close to diffraction-limited to minimize beam divergence. The laser linewidth is not a fundamental concern in incoherent detection lidar applications, and the upper limit is determined by the bandwidth of any band-pass filters used in the detection optics to suppress background radiation.

3. EXPERIMENTAL SETUP

A schematic of the two-stage master oscillator power amplifier is shown in Fig. 3. The seed oscillator (Gooch & Housego) is a high-power distributed-feedback (DFB) laser diode stabilized to 1551.23 nm during pulsed operation. It is driven with square current pulses of 15 ns duration at a pulse repetition frequency of 100 kHz, and delivers a peak power of 100 mW.

The preamplifier contains 7.5 m Er-doped single-mode fiber (Liekki Er16-8/125) that is pumped at 976 nm by a grating-stabilized single-mode diode laser delivering 900 mW. A circulator and a >99.9% reflective fiber Bragg grating (FBG) act as a narrow band-pass filter for removing amplified spontaneous emission (ASE). The FBG has a reflectance bandwidth of 0.35 nm at −0.5 dB and 0.6 nm at −35 dB, and its full reflection spectrum is shown in Fig. 4. The circulator provides high isolation of ∼100 dB between the amplification stages (50 dB per port), which blocks in-band backward ASE and protects upstream components from catastrophic damage caused by stimulated Brillouin scattering. Possible parasitic emission in the 1 μm band from Yb ions in the power amplifier is also prevented from entering the preamplifier with this setup. The forward and backward signals between the amplification stages are monitored from a 1% coupler.

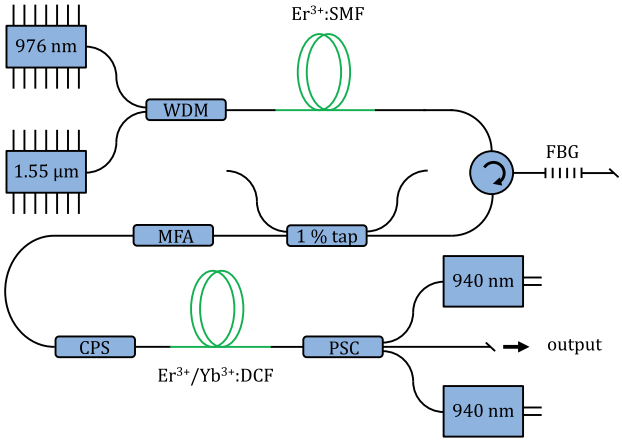

Fig. 3. Schematic of the two-stage master oscillator power amplifier containing a wavelength division multiplexer (WDM), an Er^{3+}-doped single-mode fiber (SMF), a fiber Bragg grating (FBG), a mode field adapter (MFA), a cladding power stripper (CPS), an Er^{3+}/Yb^{3+}-doped double clad fiber (DCF), and a pump-signal-combiner (PSC).

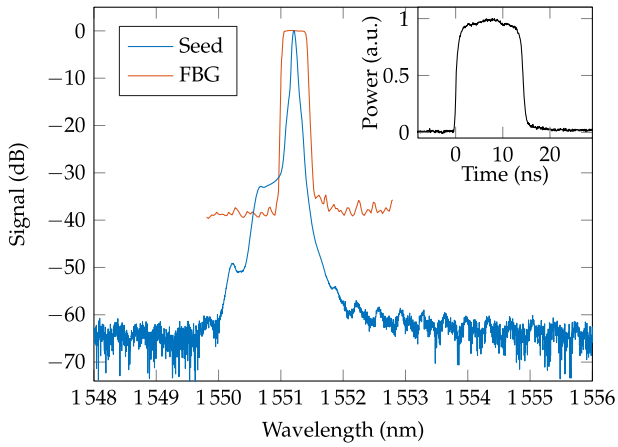

Fig. 4. Optical spectrum of the seed diode in pulsed operation (blue), measured with a resolution of 0.05 nm. The inset shows the shape of the seed pulse measured with a 1 GHz detector. The reflectance spectrum of the FBG used for filtering between amplification stages is also shown (red).

The power amplifier contains a mode field adapter, a cladding power stripper, and 2.7 m of a large-mode-area co-doped Er/Yb fiber (Nufern LMA-EYDF-25P/300-HE). The amplifier is pumped with two 940 nm fiber-coupled diode lasers delivering up to 60 W combined. Pumping is done in the backward direction through a pump-signal combiner to reduce the effective interaction length for nonlinear processes. The MOPA is terminated with a 1 m long connectorized and angle-polished delivery fiber for easy system integration.

The output is characterized with a power meter and an optical spectrum analyzer. Temporal pulse shapes are measured with a 1 GHz photodiode. A frequency chirp is obtained when operating the DFB laser in pulsed mode, which is determined from the beat frequency obtained after passing its output through an unbalanced Mach–Zehnder fiber interferometer.

The amount of ASE in the 1 μm emission band of ytterbium is measured with a power meter after removing the 1.5 μm signal with a short-pass filter. Since the ASE from erbium ions overlaps spectrally with the signal, an external acousto-optic modulator is used to time-gate the output beam in order to measure the content of 1.55 μm ASE.

The MOPA was additionally modeled using commercially available software (RP Fiber Power) that solves the time- and space-dependent rate equations for the gain media in each of the amplification stages. The Er/Yb power amplifier assumed a rate equation model and spectroscopic input parameters equal to those used in Ref. [17], while the Er-only preamplifier assumed the same equations (neglecting Yb) with spectroscopic parameters provided by the fiber manufacturer.

4. RESULTS AND DISCUSSION

A. Seed Source

Figure 4 shows the optical spectrum of the DFB seed diode when driven with 15 ns square pulses, and the inset shows the temporal pulse shape. With a high peak power of 100 mW, the pulse energy from the seed laser is estimated

to be 1.5 nJ. This means that a total amplification factor of 48 dB is required to obtain 100 μJ, which is realistically within reach using only two fiber amplification stages.

Compared to the case of continuous operation, the seed laser exhibits spectral broadening when it is pulsed due to both time variations of the drive current and thermal drift during the pulse. When interfering the pulse with a 3.5 ns delayed version of itself, a beat frequency of approximately 1 GHz is measured, which corresponds to a frequency chirp of −300 MHz/ns. The chirp originates mainly from thermal loading since the drive current is close to constant during the pulse—except for the very short transient periods when the laser is being switched (<500 ps). Observations of the interference waveforms show that the chirp is stable and repeatable from pulse to pulse; however, the chirp is not controllable without altering the drive current and thereby also the pulse shape. As expected from thermal considerations, the chirp is found to be negative through heterodyne detection by mixing the output with a local oscillator in the form of a separate continuously running DFB laser.

If the chirp is sufficiently large to shift the laser frequency outside the Brillouin gain bandwidth (∼50 MHz in silica fibers [18]) within a fraction of the pulse duration, the coherent interaction between the laser and Stokes wave is interrupted such that the SBS threshold increases. The −300 MHz/ns is indeed expected to be of a relevant magnitude for this purpose, although a comparison of the SBS threshold with the case of an unchirped pulse has not been done in this work, since the chirp is intrinsically coupled to the gain switching and cannot be removed. Results from others have shown that the SBS threshold scales linearly with chirp rate [19,20]. For instance, Ref. [19] showed a nine-fold threshold enhancement using a chirp of 5 MHz/ns with pulses of 1 μs duration from an Er/Yb fiber amplifier. In Ref. [20], a similar enhancement was achieved for an Yb fiber amplifier with 8.5 ns long pulses and a chirp of 1.19 GHz/ns. For a practical system, we consider the method of increasing the SBS threshold by utilizing the frequency chirp obtained directly from current switching as highly attractive.

B. Preamplifier

The single-stage preamplifier operates at a gain of 32 dB and provides 1.7 μJ pulses to the power amplifier after accounting for losses introduced by the spectral filtering. Figure 5 shows the optical spectrum from the preamplifier, where the filter formed by the circulator and narrow-bandwidth FBG ensures a clean spectrum at the power amplifier input by suppressing the ASE level towards the −70 dB noise floor of the measurement. The inset in Fig. 5 shows the pulse shape after the preamplifier, where slight gain saturation effects are evident compared with the pulses obtained directly from the seed laser. Simulations showed that a fairly long fiber length was favorable for operation at 1551 nm because the three-level gain medium character causes re-absorption and suppression of an otherwise strongly dominating short-wavelength ASE peak around 1530 nm.

C. Power Amplifier

Figure 6 shows the output power from the final amplifier stage, where a maximum of 13.6 W is obtained for a launched pump

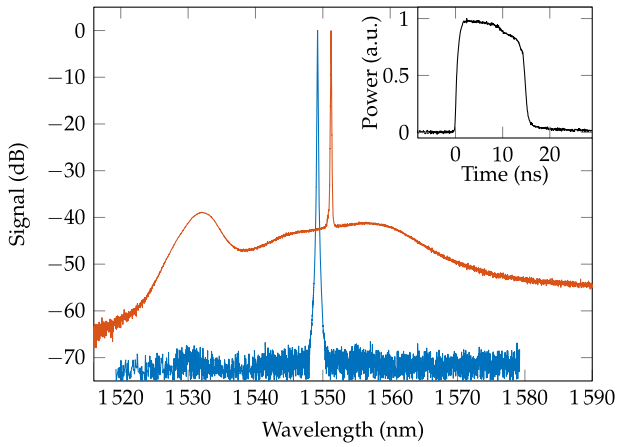

Fig. 5. Optical spectrum from the preamplifier before (red) and after (blue) spectral filtering, measured with a resolution of 0.05 nm. The filtered spectrum has been offset by −2 nm for ease of visualization. The inset shows the pulse shape measured with a 1 GHz detector.

power of 47.7 W. Also shown is the fraction of amplified spontaneous emission contained in the output from ytterbium emission around 1 μm, which is <0.1% at maximum output power. As discussed below, the content of 1.5 μm ASE from erbium emission is also negligible, and hence, the average power translates nearly directly to pulse energy by dividing with the pulse repetition frequency, and the highest energy obtained at 100 kHz becomes 135 μJ. A weak roll-off in output power is observed from around 11 W, which together with the correlated increase in 1 μm ASE is indicative of bottlenecking in the Yb-to-Er energy transfer. The bottlenecking is, however, not the determining process for limiting power scaling in the current MOPA. Instead, as further discussed below, SBS is responsible for limiting the pulse energy to 135 μJ.

At maximum output power, the optical-to-optical efficiency is 29% with respect to the launched pump power. There is a 10% total loss of pump light in the splices and the signal-pump

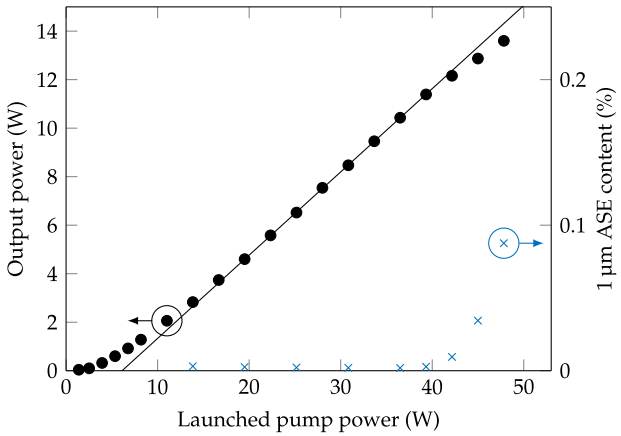

Fig. 6. Output power for different pump powers (black) and measured content of amplified spontaneous emission around 1 μm (blue). The solid line shows a fit to the linear part of the power data with a slope of 0.34.

combiner, which gives a 26% efficiency with respect to total pump power. The amount of unabsorbed pump light was not measured since it cannot be accessed in the all-fiber setup, but a pump absorption of 80% is predicted from simulations. A fit to the linear part of the power data in Fig. 6 gives a slope of 0.34. This is high compared to other reported nanosecond-pulsed 1.5 μm MOPAs in the >100 μJ class, where the highest performance in terms of pulse energy and peak powers has commonly been achieved at the expense of power efficiency, which is often limited to 10% or less [4,6].

The amount of ASE from Yb emission around 1 μm is 12 mW at the maximum pump power, i.e., less than 0.1% of the total output. This low ASE level is largely a consequence of the design choice of a 940 nm pump wavelength. As noted by others [17,21], pumping the Yb ions off-resonantly at either 915 nm or 940 nm increases the threshold for 1 μm ASE compared to pumping at 976 nm because a lower and more homogeneous inversion is obtained at the expense of needing a longer gain fiber. It is still anticipated that bottlenecking will impose a fundamental limit for average power scaling in the current MOPA design. Due to the abrupt increase in 1 μm ASE seen in Fig. 6, it is expected that significant average power scaling beyond the 13.6 W currently achieved would quickly result in detrimental amounts of 1 μm ASE. In this limit, further power scaling could be possible using Yb-free fibers.

The ASE content from Er emission was determined by time-gating the output with an acousto-optic modulator when operating the MOPA at pulse repetition frequencies (PRFs) of 25, 50, and 100 kHz. The measurements are shown in Fig. 7, where corresponding approximate ASE fractions of 0.6%, 0.3%, and 0.15% are observed. The maximum pump power that could be used at the different PRFs was limited by the onset of SBS. The error bars represent the uncertainty experienced in determining the ASE content, which was particularly large for small amounts of ASE near the detection limit of the thermal power meter used. Notably, the ASE content in Fig. 7 appears to be nearly constant with pump power within the measurement uncertainty, which is equivalent to a linear increase in ASE power with pump power. This dependence is expected in the case where the output ASE predominantly consists of ASE generated in the preamplifier that is further amplified in the power amplifier.

Simulations of the power amplifier indeed predict that negligible amounts of ASE are generated for the operating conditions used in the experiments, amounting to less than 1 mW for a signal output of 10 W. The power spectral density (PSD) of the ASE from the preamplifier (before spectral filtering) was measured with an optical spectrum analyzer to be 0.2 mW/nm close to the signal wavelength. Given the ∼0.5 nm bandwidth of the band-pass filter, this suggests that ∼0.1 mW spectrally filtered ASE from the preamplifier enters the power amplifier. The assumption that the PSD of ASE at the signal wavelength is the same as that for wavelengths in close vicinity is considered reasonable after the preamplifier, since there are no earlier amplification stages that potentially could have generated ASE that would be concealed by the strong signal. With a gain in the power amplifier of 19 dB at maximum pump power for any of the given PRFs, this ASE contribution becomes 8 mW, which, given the approximations made above, is in fair agreement with the measured ASE content in Fig. 7 of ∼15–20 mW.

A time-of-flight lidar will only make use of the energy delivered during the pulses, and thus, any power leaking as ASE will reduce the efficiency when measured against the useful output power. Through careful spectral filtering between the amplification stages, the in-band ASE content in this MOPA is kept below 1%. This is low compared to other fiber MOPAs operating at similar duty cycles, where ASE levels from several percent to tens of percent are commonly reported [4–6,8]. Advantageous from an application point of view, only a passive means of ASE filtering is used in this MOPA, as opposed to systems utilizing, e.g., temporal filtering with acousto-optic modulators between amplification stages [5].

Figure 8 shows the pulse shape at the maximum output power, where a peak power of 18 kW is estimated from scaling the area under the pulse trace to the measured energy of 135 μJ. Dynamic gain saturation in the power amplifier distorts the pulses considerably compared to the input pulses, and the full

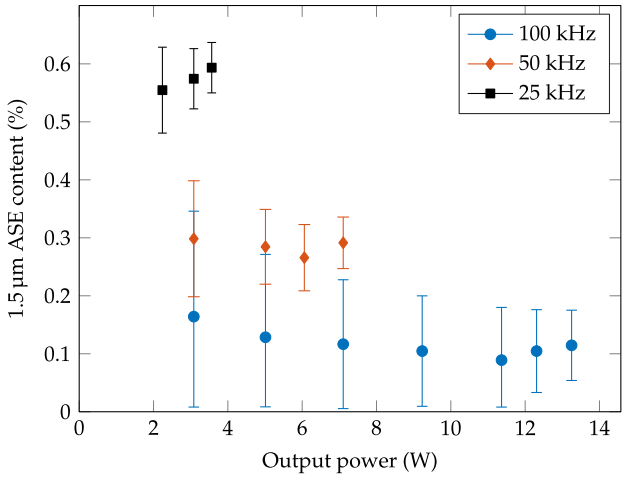

Fig. 7. Measured content of a 1.5 μm ASE in the MOPA output for operation at different pulse repetition frequencies.

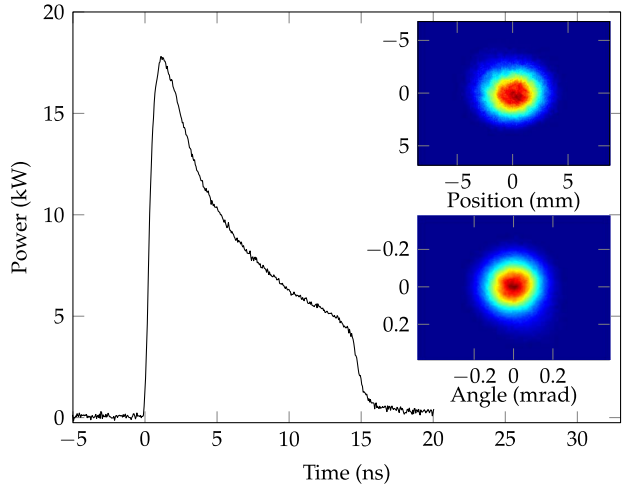

Fig. 8. Pulse shape at maximum output power. Also shown are near-field (top) and far-field (bottom) beam profiles.

width at half-maximum (FWHM) pulse duration becomes 6 ns. In applications where such deformation is unwanted, it can be compensated for by appropriately pre-shaping the seed pulses [22]. The output is very stable with negligible pulse-to-pulse fluctuations up to pulse energies of ∼110 μJ. This is an effect of using a gain-switched diode as the seed oscillator, which provides a stable output of near-identical pulses. At higher pulse energies, fluctuations at the level of a few percent emerge with the onset of SBS.

Also shown in Fig. 8 are near- and far-field beam profiles when operating at the maximum output power. From the measured second moments, 4σ beam diameters of 6.1 mm and 0.36 mrad are obtained after averaging in the x and y direction. This implies a near-diffraction-limited beam quality of $M^2 = 1.1$. A slight content of higher-order modes was evident when squeezing the delivery fiber, but the beam quality was found to vary little with such disturbance.

Figure 9 shows the optical spectrum from the power amplifier at maximum output power. A side lobe on the long-wavelength side of the central peak is observed, which as seen in Fig. 4 corresponds to a suppressed side mode of the DFB seed laser. This was confirmed by temperature-tuning the seed wavelength across the FBG filter bandwidth, which allowed amplification of side lobes at either side of the main peak. The FBG reflectance bandwidth was slightly too large to suppress all side modes at both sides of the central peak simultaneously; however, the side lobe is not a concern because its power content is negligible and also within a spectral bandwidth typically acceptable, e.g., in a direct-detection lidar application.

More significant is the spectral broadening seen as side bands symmetrically shifted from the carrier peak by 2.0 THz (∼16 nm). These features are characteristic of modulation instability (MI), which can cause significant power transfer to wavelengths outside the typical band-pass filters used in lidar systems. According to theory, the frequency shift scales with the square root of the peak power [18], corresponding to a shift where anomalous group velocity dispersion is balanced by intensity-dependent changes in refractive index. The position of the side bands was, however, found to be independent of power, and the spectral appearance is sharper than that expected from the MI gain spectrum [18]. The cause was found to be a weak parasitic reflectance in the FBG at 1535.39 nm, which seeds the modulation instability predominantly at this wavelength. This is undesirable, but can be solved by optimizing the FBG design.

Although spectral broadening from modulation instability is seen at the maximum output power, it is found that ∼95% of the power is contained within a 1 nm bandwidth from integration under the optical spectrum in Fig. 9. This fraction includes a contribution from ASE, but this is seen in Fig. 7 to constitute ∼0.15% of the output power. In other words, the out-of-band signal is predominantly attributed to nonlinear spectral broadening and not to ASE. The power fraction contained within a 1 nm bandwidth for other output powers is shown in Fig. 10. An earlier version of the MOPA [23] using a dielectric band-pass filter with a wider pass band (5 nm) and lower out-of-band extinction (20 dB) exhibited much more severe spectral broadening from modulation instability and subsequent supercontinuum generation. Hence, the careful spectral filtering used in this MOPA helps mitigate modulation instability in addition to reducing the ASE power content.

As mentioned, the pulse energy scaling of the MOPA is currently limited by the onset of stimulated Brillouin scattering. Measurements of the power propagating in the backward direction of the power amplifier are shown in Fig. 10, where the measured values correspond to the sum of contributions from 1.55 μm ASE, Rayleigh scattering of the laser light (as well as any reflections), and the Stokes signal generated by SBS. Spectral fingerprints from SBS appear in the backward signal at higher output powers, as seen in the inset in Fig. 10. At a forward power of 8.3 W, the backward signals corresponding to Rayleigh scattering and the frequency-shifted Stokes wave carry approximately equal power and are sufficiently separated to be partly resolved with the 0.05 nm spectral resolution available. The measured frequency shift of 11 GHz agrees with literature values for silica fibers [18].

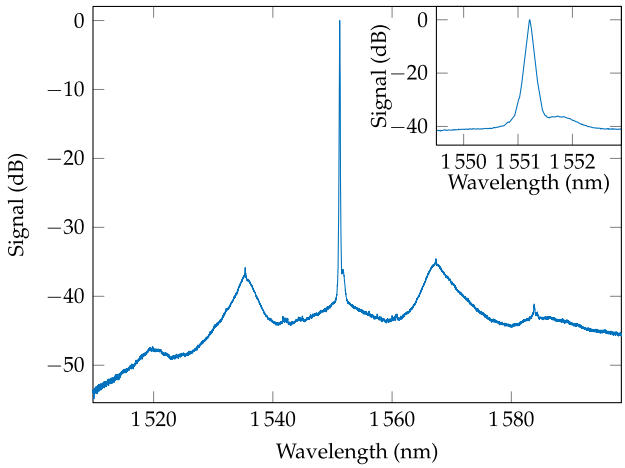

Fig. 9. Optical spectrum from the power amplifier when operating at 13.6 W, measured with 0.05 nm resolution. The inset provides a detailed view of the central peak.

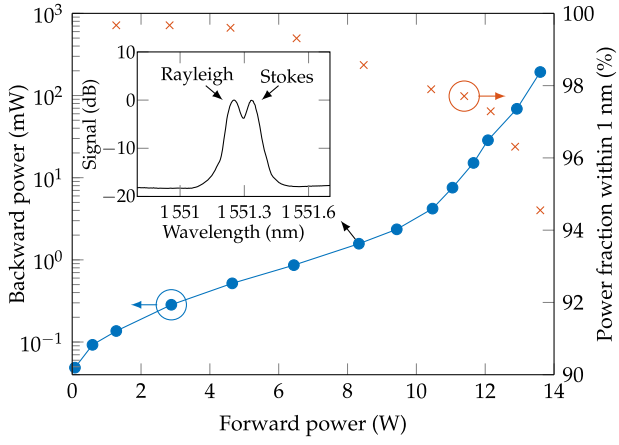

Fig. 10. Backward propagating power in the power amplifier (blue) and the fraction of the forward power contained within a bandwidth of 1 nm (red). The inset shows the backward spectrum for an output power of 8.3 W.

For output powers above ~12 W, pulse-to-pulse fluctuations become increasingly prominent, which is explained by the occasional generation of SBS pulses that deplete the gain for succeeding pulses in the power amplifier. At maximum output power, the backward signal is ~1% of the forward signal. In practice, this is found to be a reasonable operation limit for this MOPA, because further power scaling results in unstable output and excessive pulse-to-pulse fluctuations. The SBS threshold could be increased through further spectral broadening of the seed signal. This can be achieved by, for example, introducing a phase modulator, although this active control mechanism would add cost and complexity to the system.

D. Choice of Pump Wavelength

The final amplification stage is pumped at 940 nm, corresponding to a broad wing in the ytterbium absorption spectrum. This has the advantages of not requiring wavelength stabilized pump lasers and, more importantly, reducing the bottlenecking issue in Er/Yb fiber lasers, since a more even gain distribution is obtained along the gain fiber. However, it comes at the expense of requiring a longer fiber, which increases the interaction length for nonlinear processes.

For comparison purposes, the pump wavelength of the MOPA was changed to the Yb absorption peak using narrow-band diode lasers stabilized to 976 nm with volume Bragg gratings. Additionally, the gain fiber was cut to a length of 1 m, and the delivery fiber was kept short at 30 cm. In this configuration, the pulse energy could be increased to 200 μJ before the onset of SBS. Because only 18 W of power was available from the pump lasers, the pulse repetition frequency was reduced to 20 kHz in these experiments. The content of ASE at 1 μm was found to be much higher in this MOPA configuration compared to that pumped at 940 nm due to more severe bottlenecking. More than 2% of the 4.1 W output obtained at 20 kHz was measured to be 1 μm ASE, which is already at a level where significant further power scaling is impractical. In other words, the bottlenecking process is expected to prevent operation in this configuration at significantly higher PRFs than the 20 kHz used.

5. LIDAR MEASUREMENTS

With a near-diffraction-limited beam quality, an "eye-safe" operating wavelength, and a high power conversion efficiency, the described MOPA is well suited as a source for long-range scanning lidar imaging applications, and the all-fiber implementation ensures alignment-free and reliable operation under harsh conditions. Furthermore, the diode-seeded MOPA architecture ensures adaptivity and easy integration into a lidar system, since pulse durations and repetition frequencies can be adjusted electronically to match the detection bandwidth and the desired operating pulse repetition frequency.

The MOPA was installed in an in-house-developed scanning lidar system and used for 3D imaging. Figure 11 shows the resulting 3D images of a scene that contains objects at ranges up to 10 km, while Fig. 12 shows the number of detected return pulses as a function of distance for the same recordings. A Gaussian filter with a width of 200 m (FWe^{-2}M) has been applied to smooth the data in Fig. 12 for visual purposes. This reduces the apparent range resolution, which in the experiments was found to be <1 m, given reasonable SNRs. The pulse repetition frequency was set to 89 kHz during the measurements, and images were recorded when operating at pulse energies of 10, 47, and 120 μJ. The detection threshold for return pulses was set to 50 aJ, which corresponds to the threshold assumed in the calculations of detection ranges in Section 2. The atmospheric visibility during the measurements is not known, but the optical image in Fig. 11 suggests a visibility of significantly more than 10 km at visible wavelengths, since the hillside at this distance is seen with a high contrast (i.e., well above 2%) against the sky. When accounting for the wavelength dependence of the atmospheric visibility [14],

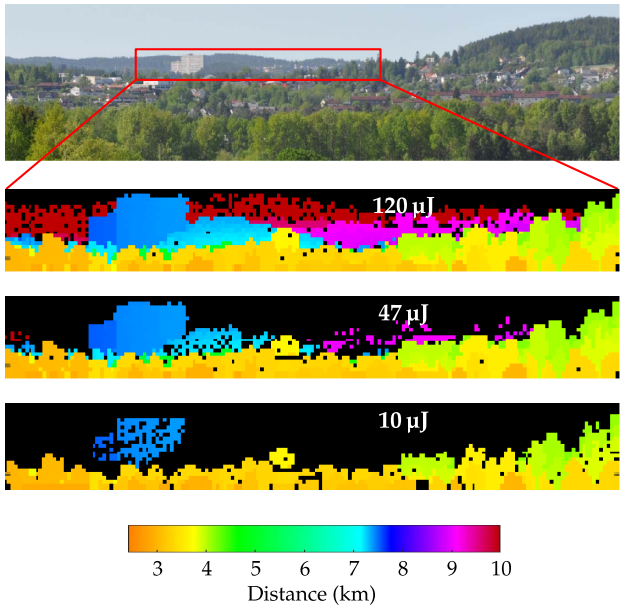

Fig. 11. 3D images recorded with the MOPA installed in a scanning lidar system for different pulse energies as noted in the images. A camera image of the scene is shown where the capture frame for the lidar images is outlined.

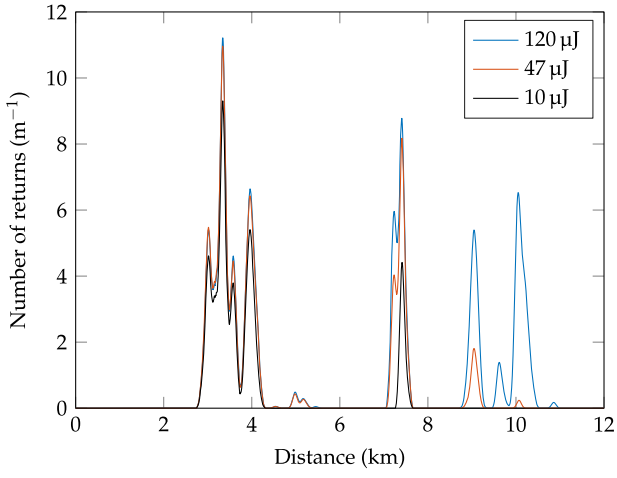

Fig. 12. Number of detected return pulses as a function of distance for the lidar images in Fig. 11.

we deduce that the visibility at the laser wavelength was high—most likely 50 km or above.

It is noted that the detection ranges observed in Fig. 11 and those computed from Eq. (1) are expected to differ due to the assumption of a constant 10% target reflectivity. Deviations from this reflectivity can, for instance, explain the partial detection of the buildings at 7.5 km, even with 10 μJ pulses, for which a maximum detection range of 2–4 km is expected from Fig. 2. Nevertheless, as approximate estimates, the detection ranges observed in the lidar measurements are in fair agreement with the calculations in Section 2. For instance, Figs. 11 and 12 show that there is only a small difference in returns from the objects at the 2–4 km range, whereas only the image recorded at 120 μJ shows more than a few return pulses from objects at 9 km and beyond.

To summarize, these experiments demonstrate that 100 μJ class fiber lasers represent a relevant technology for scanning lidar applications with detection ranges of several km.

6. CONCLUSION

In conclusion, we have presented a nanosecond-pulsed 1.55 μm Er/Yb master oscillator power amplifier with high pulse energy and peak power suitable for applications in 3D lidar imaging with detection ranges of several km. The MOPA is seeded by a high-power distributed-feedback diode laser followed by two fiber amplification stages built from commercially available components. It delivers pulses of 6 ns duration (FWHM) with 135 μJ energy at a pulse repetition frequency of 100 kHz, limited by stimulated Brillouin scattering. The output has a near-diffraction-limited beam quality of $M^2 = 1.1$, and careful spectral filtering between the amplification stages ensures that 95% of the power is spectrally contained within a 1 nm bandwidth and >99% of the average power is temporally contained in the pulses. Combined with an optical-to-optical efficiency of 29% and a robust all-fiber design, this MOPA is well suited for field operation, and we have demonstrated 3D imaging at the several-kilometer range with the source installed in an in-house-developed scanning lidar system.

Funding. UNIK-foundation.

Acknowledgment. L. G. H. is funded by a PhD grant from the UNIK-foundation.

REFERENCES

1. P. F. McManamon, "Review of ladar: a historic, yet emerging, sensor technology with rich phenomenology," Opt. Eng. **51**, 060901 (2012).
2. National Research Council, *Laser Radar: Progress and Opportunities in Active Electro-Optical Sensing* (The National Academies, 2014).
3. P. F. McManamon, *Field Guide to Lidar* (SPIE, 2015).
4. L. Kotov, M. Likhachev, M. Bubnov, O. Medvedkov, D. Lipatov, A. Guryanov, K. Zaytsev, M. Jossent, and S. Février, "Millijoule pulse energy 100-nanosecond Er-doped fiber laser," Opt. Lett. **40**, 1189–1192 (2015).
5. I. Pavlov, E. Dülgergil, E. Ilbey, and F. Ö. Ilday, "Diffraction-limited, 10-W, 5-ns, 100-kHz, all-fiber laser at 1.55 μm," Opt. Lett. **39**, 2695–2698 (2014).
6. Z. Zhao, H. Xuan, H. Igarashi, S. Ito, K. Kakizaki, and Y. Kobayashi, "Single frequency, 5 ns, 200 μJ, 1553 nm fiber laser using silica based Er-doped fiber," Opt. Express **23**, 29764–29771 (2015).
7. E. L. Lim, S. U. Alam, and D. J. Richardson, "High-energy, in-band pumped erbium doped fiber amplifiers," Opt. Express **20**, 18803–18818 (2012).
8. V. V. Dvoyrin, D. Klimentov, J. O. Klepsvik, I. V. Mazaeva, and I. T. Sorokina, "Multi-kilowatt peak power nanosecond Er-doped fiber laser," IEEE Photon. Technol. Lett. **28**, 2772–2775 (2016).
9. K. Guo, X. Wang, P. Zhou, and B. Shu, "4 kW peak power, eye-safe all-fiber master-oscillator power amplifier employing Yb-free Er-doped fiber," Appl. Opt. **54**, 504–508 (2015).
10. S. Desmoulins and F. Teodoro, "High-gain Er-doped fiber amplifier generating eye-safe MW peak-power, mJ-energy pulses," Opt. Express **16**, 2431–2437 (2008).
11. W. Lee, J. Geng, S. Jiang, and A. W. Yu, "1.8 mJ, 3.5 kW single-frequency optical pulses at 1572 nm generated from an all-fiber MOPA system," Opt. Lett. **43**, 2264–2267 (2018).
12. J. Yun, C. Gao, S. Zhu, C. Sun, H. He, L. Feng, L. Dong, and L. Niu, "High-peak-power, single-mode, nanosecond pulsed, all-fiber laser for high resolution 3D imaging LIDAR system," Chin. Opt. Lett. **10**, 121402 (2012).
13. L. S. Rothman, I. E. Gordon, Y. Babikov, A. Barbe, D. Chris Benner, P. F. Bernath, M. Birk, L. Bizzocchi, V. Boudon, L. R. Brown, A. Campargue, K. Chance, E. A. Cohen, L. H. Coudert, V. M. Devi, B. J. Drouin, A. Faytl, J.-M. Flaud, R. R. Gamache, J. J. Harrison, J.-M. Hartmann, C. Hill, J. T. Hodges, D. Jacquemart, A. Jolly, J. Lamouroux, R. J. Le Roy, G. Li, D. A. Long, O. M. Lyulin, C. J. Mackie, S. T. Massie, S. Mikhailenko, H. S. P. Müller, O. V. Naumenko, A. V. Nikitin, J. Orphal, V. Perevalov, A. Perrin, E. R. Polovtseva, C. Richard, M. A. H. Smith, E. Starikova, K. Sung, S. Tashkun, J. Tennyson, G. C. Toon, V. G. Tyuterev, and G. Wagner, "The HITRAN2012 molecular spectroscopic database," J. Quant. Spectrosc. Radiat. Transfer **130**, 4–50 (2013).
14. I. I. Kim, B. McArthur, and E. J. Korevaar, "Comparison of laser beam propagation at 785 nm and 1550 nm in fog and haze for optical wireless communications," Proc. SPIE **4214**, 26–37 (2001).
15. J. A. Overbeck, M. S. Salisbury, M. B. Mark, and E. A. Watson, "Required energy for a laser radar system incorporating a fiber amplifier or an avalanche photodiode," Appl. Opt. **34**, 7724–7730 (1995).
16. R. D. Richmond and S. C. Cain, *Direct-Detection LADAR Systems* (SPIE, 2010).
17. O. D. Varona, W. Fittkau, P. Booker, T. Theeg, M. Steinke, D. Kracht, J. Neumann, and P. Wessels, "Single-frequency fiber amplifier at 1.5 μm with 100 W in the linearly-polarized TEM_{00} mode for next-generation gravitational wave detectors," Opt. Express **25**, 24880–24892 (2017).
18. G. P. Agrawal, *Nonlinear Fiber Optics*, 5th ed. (Academic, 2013).
19. J. O. White, D. Engin, M. Akbulut, G. Rakuljic, N. Satyan, A. Vasilyev, and A. Yariv, "Chirped laser seeding for SBS suppression in a 100-W pulsed erbium fiber amplifier," IEEE J. Quantum Electron. **51**, 6800110 (2015).
20. P. I. Ionov and T. S. Rose, "SBS reduction in nanosecond fiber amplifiers by frequency chirping," Opt. Express **24**, 13763–13777 (2016).
21. Q. Han, J. Ning, and Z. Sheng, "Numerical investigation of the ASE and power scaling of cladding-pumped Er-Yb codoped fiber amplifiers," IEEE J. Quantum Electron. **46**, 1535–1541 (2010).
22. D. N. Schimpf, C. Ruchert, D. Nodop, J. Limpert, A. Tünnermann, and F. Salin, "Compensation of pulse-distortion in saturated laser amplifiers," Opt. Express **16**, 17637–17646 (2008).
23. L. G. Holmen, G. Rustad, and M. W. Haakestad, "Robust eye-safe pulsed fiber laser source for 3D ladar applications," Proc. SPIE **10434**, 104340N (2017).